Lifetime measurements of ^{162}Er: Evolution of collectivity in the rare-earth region

L. Knafla,[1,*] G. Häfner,[2,1] J. Jolie,[1] J.-M. Régis,[1] V. Karayonchev,[1] A. Blazhev,[1] A. Esmaylzadeh,[1] C. Fransen,[1] A. Goldkuhle,[1] S. Herb,[1] C. Müller-Gatermann,[1,†] N. Warr,[1] and K. O. Zell[1]

[1]*Universität zu Köln, Mathematisch-Naturwissenschaftliche Fakultät, Institut für Kernphysik, 50937 Köln, Germany*

[2]*Université Paris-Saclay, CNRS/IN2P3, IJCLab, F-91405 Orsay, France*

(Received 1 July 2020; accepted 31 August 2020; published 9 October 2020)

Lifetimes of low-lying yrast states in ^{162}Er are measured using the electronic γ-γ fast-timing technique. Excited states were populated in a ^{154}Sm(^{12}C, $4n$) ^{162}Er fusion-evaporation reaction and γ rays were detected in a combined setup of high purity germanium and $LaBr_3$(Ce) scintillation detectors. The lifetimes of the 4_1^+ and 6_1^+ states are determined for the first time and the lifetimes of the 2_1^+ and 7^- states are remeasured with higher precision. Reduced transition probabilities are extracted and well reproduced by theoretical calculations in the framework of the confined β soft model and the interacting boson model.

DOI: 10.1103/PhysRevC.102.044310

I. INTRODUCTION

The study of deformed nuclei in the rare-earth midshell region ($Z = 66$, $N = 104$) is important in understanding the complete picture of the quantum many-body system. It is well established that the observables for the degree of quadrupole collectivity in even-even nuclei, e.g., $B(E2; 2_1^+ \rightarrow 0_1^+)$ values, scales with the product of valence protons, N_π, and valence neutrons, N_ν [1]. Throughout the transition from spherical to axially deformed shape, the nature of low-lying excitations changes from vibrational to rotational, with accompanying changes in the 2_1^+ level energy and changes in reduced $E2$ transition probabilities [2].

Critical-point symmetries in nuclear structure provide an analytic description of nuclear structure properties of nuclei in the transitional region [3–20]. Starting from the Bohr Hamiltonian [21], Pietralla and Gorbachenko introduced the confined beta soft (CBS) model [11] for prolate axially symmetric ($\gamma \approx 0°$) solutions between X(5) [4] and SU(3). With a focus on the β degree of freedom, the potential $v(\beta)$ is considered an infinite square well with dynamic boundaries from β_m to β_M, where $0 \leqslant \beta_m < \beta_M$. The ratio $r_\beta = \beta_m/\beta_M \in [0, 1)$ uniquely specifies the stiffness of the potential and, thus, the structural evolution from the transitional region ($r_\beta = 0$) to the rigid rotor ($r_\beta \rightarrow 1$).

The nucleus ^{162}Er ($N = 94$) is bordering the transitional $N \approx 90$ region and one of the first nuclei in the erbium chain of isotopes to exhibit well-deformed rotational structure but expected to show signs of β-softness [22]. The half-life of the 2_1^+ state in ^{162}Er has been measured previously. It was directly measured using β-γ timing following the electron-capture decay of ^{162}Tm [23,24] and deduced within a Coulomb excitation study [25]. The evolution of the $B(E2; 2_1^+ \rightarrow 0_1^+)$ values in the chain of Er isotopes suggest a rather smooth development of collectivity as a function of neutron number, as it is expected from the $N_\pi N_\nu$ scheme. No lifetimes in the ground-state band with $J > 2$ are known in ^{162}Er. To describe the details of the nuclear structure of this nucleus an experiment to measure lifetimes up to the 8_1^+ state has been performed and will be discussed in this work.

A multitude of K isomers [26], where K is the projection of angular momentum on the symmetry axis of the deformed nuclear shape, is known in the rare-earth region. Transitions where the change in K quantum number exceeds the multipole order λ are called K forbidden and have a hindered decay rate. The degree of forbiddenness is described by the reduced hindrance factor f_ν [27], where $\nu = \Delta K - \lambda$. In ^{162}Er, a $K^\pi = 7^-$ isomer decaying to the ground-state band exists with a reduced hindrance of $f_\nu = 33.1(13)$ [28]. This state was interpreted as a two-quasiparticle isomer with a $\pi\, 7/2^-[523]\pi\, 7/2^+[404]$ configuration. A dominant K mixing in this isomer was suggested due to the near constancy of the reduced hindrance over the full moment-of-inertia range. The lifetime of the isomer is remeasured in this work, significantly reducing its uncertainty.

II. EXPERIMENTAL DETAILS

The experiment was performed at the 10 MV FN-Tandem accelerator of the Institute for Nuclear Physics at the University of Cologne. Excited states in ^{162}Er were populated in the ^{154}Sm(^{12}C, $4n$) ^{162}Er fusion-evaporation reaction at a beam energy of 62 MeV. The enriched ^{154}Sm target with a thickness of 0.9 mg/cm^2 was supported by a 2.2 mg/cm^2 thick tantalum backing. The de-excitation via γ rays was measured with the HORUS spectrometer [29] equipped with eight high-purity germanium (hereafter denoted as 'HPGe') detectors and eight 1.5 in. × 1.5 in. $LaBr_3$(Ce) scintillation detectors (hereafter

*Corresponding author: lknafla@ikp.uni-koeln.de

†Present address: Argonne National Laboratory, 9700 South Cass Ave, Argonne, IL 60439, USA.

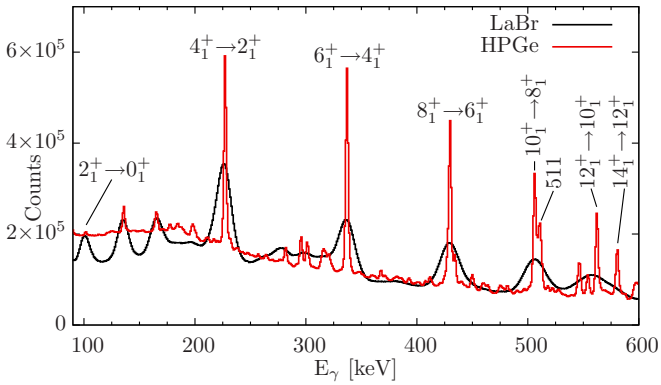

FIG. 1. Projections of threefold $\gamma\gamma\gamma$-coincidence spectra measured during this experiment. The HPGe spectrum is generated using Ge-LaBr-Ge events and the LaBr spectrum is generated using Ge-LaBr-LaBr events. The dominant transitions in ^{162}Er are labeled.

denoted as 'LaBr'). In this setup the HPGe detectors were used to select a γ-ray cascade of interest and the LaBr detectors were used to precisely measure the time difference between the populating and depopulating transitions of an excited state.

The full projection of HPGe and LaBr threefold coincidences measured during this experiment is shown in Fig. 1 and the strongest transitions in ^{162}Er are labeled. The $4n$ evaporation channel dominates the spectrum with a clean identification of transitions in ^{162}Er up to high spins. To optimize efficiency, the LaBr detectors were moved as close as possible to the target position, without obstructing the HPGe detectors. Six out of eight LaBr detectors were surrounded by bismuth germanate scintillators to suppress the Compton background. The front windows of the HPGe detectors were equipped with absorber material consisting of a layer of lead and copper to reduce the count rate of low energetic γ rays and especially x rays. In effect, this also strongly reduces the detection of the $2_1^+ \rightarrow 0_1^+$ (102 keV) transition which is only visible in the LaBr energy projection (see Fig. 1).

The anode output of the LaBr detectors is connected to a constant-fraction discriminator (CFD) to provide a timing signal, while the energy information is delivered by the pulse height of the dynode signal. The CFD outputs are connected to time-to-amplitude converters (TAC) and deliver the start or stop signal for time difference measurements. LaBr and HPGe energy signals, as well as the TACs output signals are connected to digital gamma finder (DGF) modules. An in-depth description of the electronic circuit and its modules is discussed in Ref. [30].

III. LIFETIME ANALYSIS

Lifetimes of excited states in ^{162}Er are determined using the well-established generalized centroid difference (GCD) method [31]. The method relies on the direct measurement of the time difference between γ rays populating and depopulating a given state.

Considering a feeder-decay cascade with respect to a state of interest, the setup generates two independent time distributions. If a detector connected to the start-input of a TAC observes the γ ray feeding the state of interest and a stop detector detects the decaying transition, a so-called delayed time distribution is generated. If the populating and depopulating γ rays are detected in reverse, the so-called antidelayed time distribution is generated.

Under the assumption of no background contributions, the delayed time distribution is defined as the convolution of the prompt-response function (PRF) of the system and an exponential decay:

$$D(t) = n\lambda \int_{-\infty}^{t} \mathrm{PRF}(t' - t_0) e^{-\lambda(t-t')} dt' + n_r, \qquad \lambda = 1/\tau, \tag{1}$$

where n is the number of coincidences in the time distribution, n_r is the number of random counts, and τ is the mean lifetime of the state connected by the feeder-decay cascade. For further details on the definition and characteristics of the independent time distributions see Refs. [30,31].

If the lifetime of a given state is larger than the width of the PRF, a slope can be seen in time spectrum which is attributed to the decay constant λ. However, if the lifetime is shorter, no exponential decay is visible and the centroid of the time distribution is shifted by the mean lifetime from the centroid of the PRF [32]. With the GCD method the lifetime of the state of interest can be extracted from the centroid difference between the independent delayed and antidelayed time distribution while correcting for the time response of the system [31]:

$$2\tau = \Delta C(E_{\mathrm{feeder}}, E_{\mathrm{decay}}) - \mathrm{PRD}(E_{\mathrm{feeder}}, E_{\mathrm{decay}}). \tag{2}$$

The centroid difference $\Delta\mathrm{C}(E_{\mathrm{feeder}}, E_{\mathrm{decay}})$ is defined as the difference between the centroid of the delayed and antidelayed time distribution and can be directly determined from sorted experimental data. The prompt response difference (PRD) is the difference between the centroids of the PRF for the delayed and antidelayed time distribution. The PRD describes the combined γ-γ time response of the system and has to be calibrated and determined experimentally for a given setup. This is done using a ^{152}Eu source and selecting γ-ray cascades with known lifetimes. For a detailed description of the PRD calibration procedure the reader is referred to Ref. [30]. The final calibrated PRD curve is shown in Fig. 2 and is fitted using the following function [30]:

$$\mathrm{PRD}(E_\gamma) = \frac{a}{\sqrt{E_\gamma + b}} + cE_\gamma + d. \tag{3}$$

The uncertainty was determined from the statistical fluctuation of the fit residuals and amounts to 5 ps corresponding to 2σ.

Equation (2) only holds if no background is influencing the measured time distributions. This is seldom the case, as Compton background from coincident γ rays cannot be fully eliminated. These Compton scattered γ rays originate from other transitions and show different, energy-dependent time response. This makes the correction for the time correlated background, influencing the measured centroid difference

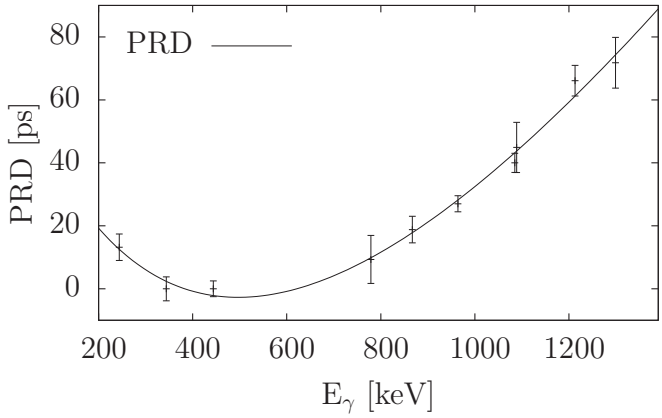

FIG. 2. Calibrated PRD curve relative to the reference energy of $E_{\text{ref}} = 344$ keV. The data points obtained from other reference energies are shifted in parallel. The standard deviation is calculated and results in a PRD uncertainty of 5 ps.

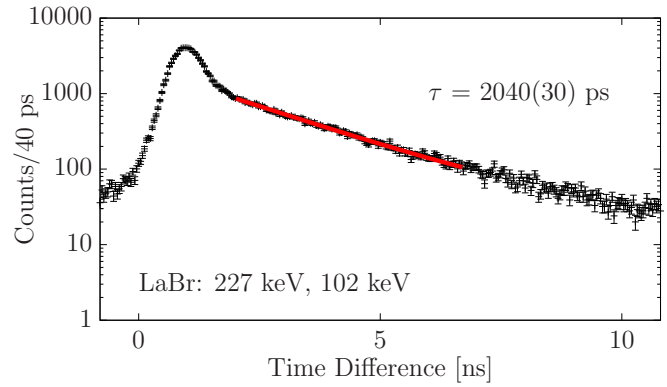

FIG. 3. Time distribution obtained after applying LaBr gates on the $4_1^+ \rightarrow 2_1^+$ (227 keV) and $2_1^+ \rightarrow 0_1^+$ (102 keV) transitions. The fit to determine the lifetime of the 2_1^+ is shown in red.

ΔC_{exp}, a necessity. It has been shown that a precise correction of background time influence can be performed by applying an analytic correction term (t_c) without subtracting any time correlated data [33]:

$$\Delta C_{FEP} = \Delta C_{\text{exp}} + t_c = \Delta C_{\text{exp}} + \frac{\Delta C_{\text{exp}} - \Delta C_{bg}}{p/b}. \quad (4)$$

In Eq. (4), the centroid difference of the full energy peak ΔC_{FEP} is obtained by correcting the measured centroid difference ΔC_{exp} for the background time responses ΔC_{bg} weighted by the peak-to-background ratio p/b. The background time response at position of the FEP is interpolated from measured background time response around the peak of interest.

As both peaks of interest are influenced by background, the background related timing influence from both peaks needs to be corrected for [34]

$$\tilde{t}_c(E_f, E_d) = \frac{p/b(E_d)t_c(E_f) + p/b(E_f)t_c(E_d)}{p/b(E_d) + p/b(E_f)}. \quad (5)$$

The feeding and decaying transitions are denoted by the subscripts f and d, respectively. Equation (5) takes into account possibly large differences in peak-to-background ratios between both peaks of interest and corresponds to a weighted average. To calculate the background corrected centroid difference ΔC_{FEP}, t_c is replaced by $\tilde{t}_c(E_f, E_d)$ in Eq. (4). The final uncertainty of the lifetime is calculated from Gaussian error propagation.

IV. RESULTS

A. Remeasurement of the 2_1^+ lifetime

Previous lifetime measurements of the 2_1^+ state either have a large uncertainty ($\tau = 2200(400)$ ps [24]) or barely lie within a 2σ interval ($\tau = 1690(140)$ ps [23], $\tau = 1980(30)$ ps [25], $\tau = 2036(104)$ ps [35]) motivating a remeasurement of this lifetime.

Due to the long lifetime, the measured time spectrum shows the exponential decay expressed as a slope to one side of the spectrum. Fitting an exponential function to the slope, taking a constant background into account, yields the lifetime according to Eq. (1).

The time spectrum shown in Fig. 3 is generated by applying narrow LaBr gates on the $4_1^+ \rightarrow 2_1^+$ (227 keV) and $2_1^+ \rightarrow 0_1^+$ (102 keV) transitions. Additionally, the independent antidelayed time spectrum has been mirrored and added to the delayed time spectrum to increase statistics. The integral of the summed time distribution amounts to about 10^5 counts. The fit interval is restricted to the area where the decay of the 2_1^+ state dominates to minimize the influence of slow background components. The lifetime is determined by varying the fit interval and taking the median of multiple fits. The uncertainty is calculated from 1σ standard deviation.

The final lifetime following this analysis amounts to 2040(30) ps. Note that the lifetime does not match the weighted average [$\tau = 1974(28)$ ps] of the lifetimes from Refs. [23–25,35] due to the measurement reported in Ref. [23]. The result is consistent with the measurements from Refs. [24,25,35].

B. Lifetime measurement of low-lying yrast states

The lifetime analysis of the low-lying yrast states is performed using the GCD method. For this analysis triple HPGe-LaBr-LaBr coincidences are used. Applying a HPGe gate to a γ ray coincident to the cascade of interest cleans up and simplifies the LaBr spectra while reducing the background significantly. Applying LaBr gates on the feeding and decaying transition of the state of interest then generates the delayed and antidelayed time spectra. To confirm that the timing gates are not contaminated by coincident γ rays, triple HPGe-LaBr-HPGe coincidences are used, utilizing the resolution of the HPGe detectors to investigate the energy spectra.

To measure the lifetime of the 4_1^+ state, the $6_1^+ \rightarrow 4_1^+ \rightarrow 2_1^+$ (337-227 keV) cascade is used with an additional HPGe gate placed on the $8_1^+ \rightarrow 6_1^+$ (430 keV) transition. The situation after applying a HPGe and a LaBr gate on the feeding (decaying) transition, respectively, is shown in Fig. 4(a) and 4(b). The gated spectra show no contamination close to the peaks corresponding to the feeding and decaying transition.

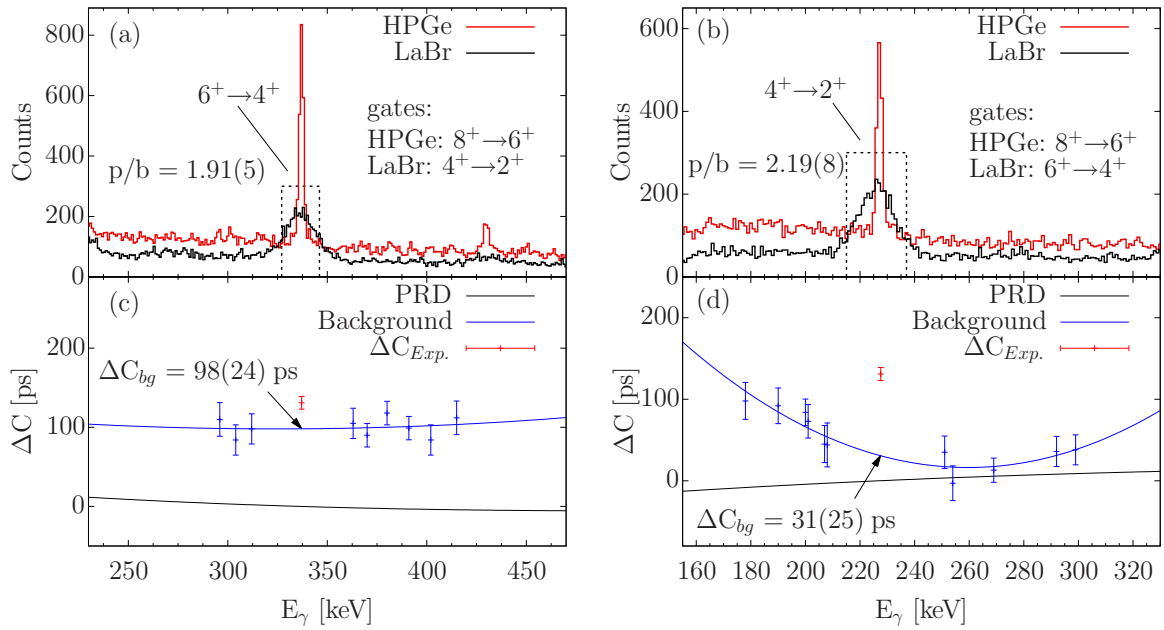

FIG. 4. Analysis of the 4^+ state. (a,b) Double gated HPGe and LaBr energy spectrum with HPGe gate on the $8_1^+ \rightarrow 6_1^+$ (430 keV) transition and LaBr gate on (a) $4_1^+ \rightarrow 2_1^+$ (227 keV) or (b) $6_1^+ \rightarrow 4_1^+$ (337 keV). The peaks of interest are well separated from any disturbing transitions. The second LaBr gate to generate the time difference spectra is indicated by dashed lines. (c,d) Measured centroid difference (red) and PRD curve (black) shifted to the energy of the applied LaBr gate. The measured background time response and corresponding interpolation is also shown (blue). (c,d) The PRD curve is mirror symmetric with respect to a start-stop inversion of a γ-γ cascade [30].

After applying the second LaBr gate the delayed and antidelayed time distributions are generated [see Fig. 6(a)]. These time distributions are directly influenced by time correlated background affecting both peaks of interest. The interpolation of the background time response is performed separately for each peak and is shown in Fig. 4(c) and 4(d). After performing the analytic background correction according to Eq. (4), the lifetime of the 4_1^+ state is calculated from Eq. (2). With a PRD$(337, 227) = -12(5)$ ps the lifetime of the 4_1^+ state amounts to $\tau(4_1^+) = 87(6)$ ps.

The lifetime of the 6_1^+ state is measured via the $8_1^+ \rightarrow 6_1^+ \rightarrow 4_1^+$ (430-337 keV) cascade with an additional HPGe gate applied to the $4_1^+ \rightarrow 2_1^+$ (227 keV) transition. The gated spectra, background correction and PRD are shown in

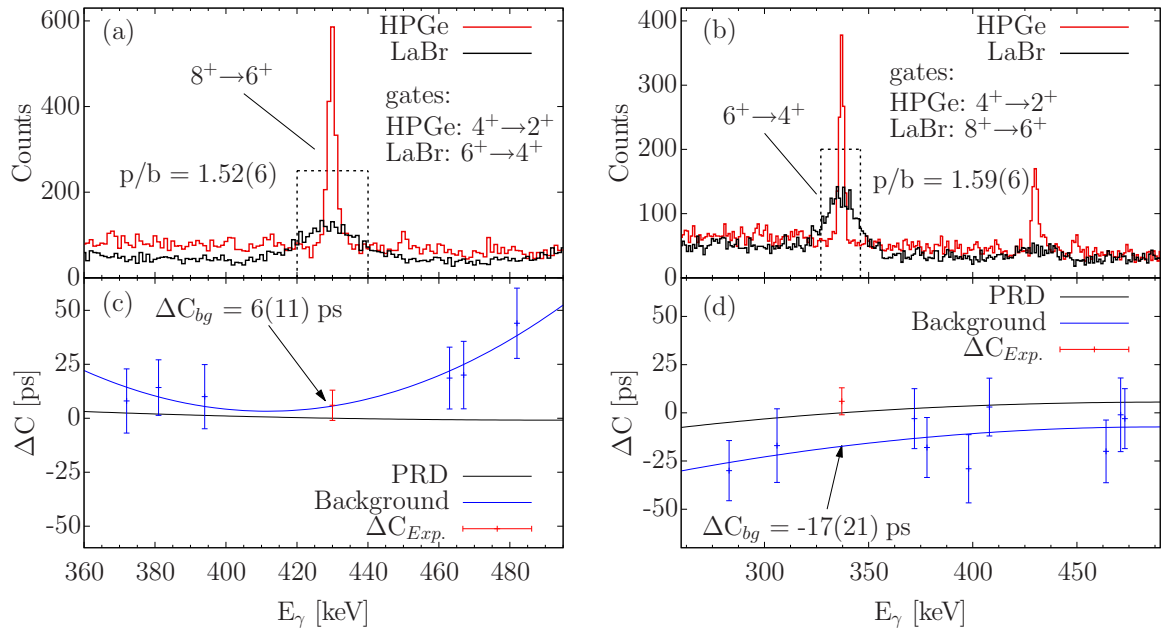

FIG. 5. Same as Fig. 4 but for the 6_1^+ state. The double gate spectra in (a,b) are generated by applying a HPGe gate on the $4_1^+ \rightarrow 2_1^+$ (227 keV) transition and a LaBr gate on (a) $6_1^+ \rightarrow 4_1^+$ (337 keV) or (b) $8_1^+ \rightarrow 6_1^+$ (430 keV).

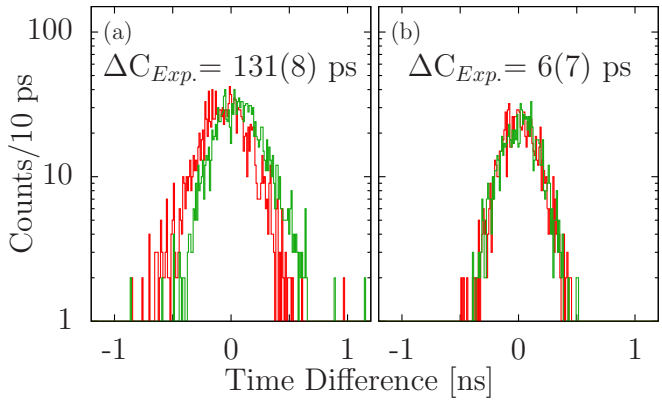

FIG. 6. Delayed (green) and antidelayed (red) time distribution as well as the centroid difference ΔC_{exp} for the lifetime measurement of the (a) 4_1^+ and (b) 6_1^+ state. The applied gates are discussed in the text.

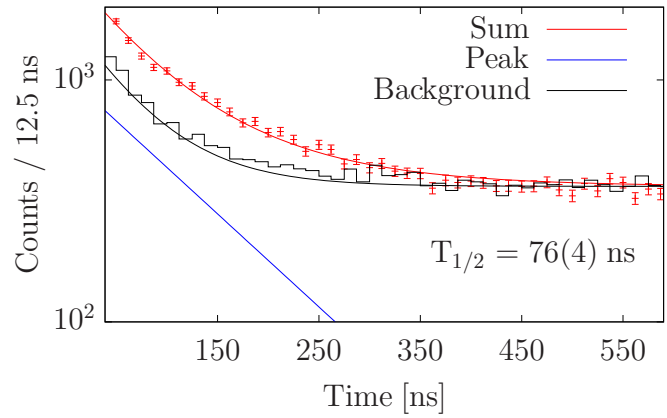

FIG. 7. DGF time-stamp distribution for the 1360 keV transition measured by the HPGe detectors. The spectrum is fitted with a sum (red) of an exponential peak component (blue) and an exponential plus constant background component (black). The time-dependent background is shown additionally as a black histogram from gates around the 1360 keV transition.

Fig. 5 and the delayed and antidelayed time spectra are shown in Fig. 6(b). With a PRD(430, 337) = 5(5) ps this analysis yields $\tau(6_1^+) = 9(6)$ ps. The lifetime of the 8^+ state is below the limit of the sensitivity of the GCD method. While the state of interest can be accessed via the $10_1^+ \rightarrow 8_1^+ \rightarrow 6_1^+$ (506-430 keV) cascade, trying to determine a centroid difference shows no centroid shift distinguishable from the PRD. Under these circumstances only an upper limit of 5 ps can be estimated based on the uncertainty of the PRD curve.

C. Half-life of the $7^{(-)}$ isomer

An isomer with a $K^\pi = 7^-$ assignment at 2027 keV has been observed to decay into the ground state band via 1360 keV and 930 keV transitions [28]. The half-life of the isomer is remeasured by analyzing the HPGe time-stamp distribution of the 1360 keV γ ray decaying into the 6_1^+ state. The 930 keV transition is not used because of its lower intensity and a contaminant 929 keV transition. The non-subtracted time distribution can be seen in Fig. 7. It is fitted with a sum of a time-dependent background and an exponential decay according to the method described in Ref. [36]. The exponential background accounts for contributions such as Compton scattered events that may enter the HPGe gate and influence the time distribution. The resulting half-life amounts to 76(4) ns which is in accordance to the previously reported value of 88(16) ns while significantly reducing its uncertainty. The uncertainty is determined by systematically varying the fit region and background components of the fit. The new lifetime with lower uncertainty changes the reduced hindrance factor for this K isomer from $f_\nu = 33.1(13)$ [28] to $f_\nu = 32.1(3)$. Compared to the previous result this indicates a slightly increased degree of Coriolis K mixing of the isomer within the ground-state band [37].

V. DISCUSSION

A. Systematics of $B(E2)$ values and quadrupole deformation

Table I summarizes the results from the lifetime measurements of low-lying yrast states. Reduced transition probabilities are deduced and compared to different theoretical calculations which will be discussed in the following sections.

Figure 8(a) shows the $B(E2)$ values for low-lying yrast transitions up to $J = 8$ as a function of neutron number for $^{156-170}$Er. From the $N_\pi N_\nu$ scheme an increase of $B(E2; 2_1^+ \rightarrow 0_1^+)$ transition strength accompanied by a lowering of 2_1^+ energies up to neutron mid shell at $N = 104$ is expected. Instead, the $B(E2; 2_1^+ \rightarrow 0_1^+)$ values reach their maximum around $N = 98$ and start to slightly decrease afterwards while the $E(2_1^+)$ continuously decrease with a minimum at neutron mid shell (see Table II). A similar phenomenon was observed in the ^{66}Dy isotopic chain where a minimum of 2_1^+ energies suggested a maximum of collectivity at $N = 98$ but the evolution of collectivity was shown to follow the predicted saturation [44,45]. No $B(E2; 2_1^+ \rightarrow 0_1^+)$ value for ^{172}Er is known, that would put this trend of the erbium isotopes in the context of a saturation effect up to midshell [46]. To further shed light on this phenomenon the quadrupole deformation is determined from the $B(E2)$ values. The quadrupole moment Q_t can be obtained from the $B(E2)$ via [47]:

$$B(E2) \downarrow = \frac{5}{16\pi} Q_t^2 |\langle IK20|(I-2)K\rangle|^2, \qquad (6)$$

TABLE I. Lifetimes of excited states measured in this work. For $A = 162$, 1 W.u. corresponds to 52.5 e^2fm^4. The last two columns denote results from theoretical calculations within the CBS and IBM-1 framework. See text for details.

	Ex	τ		E_γ	$B(E2)$ [W.u.]		
J^π	[keV]	[ps]	$J_i^\pi \rightarrow J_f^\pi$	[keV]	exp	CBS	IBM
2_1^+	102.0	2040(30)	$2_1^+ \rightarrow 0_1^+$	102	185(3)	185	185
4_1^+	329.6	87(6)	$4_1^+ \rightarrow 2_1^+$	228	250^{+20}_{-15}	272	266
6_1^+	666.7	9(6)	$6_1^+ \rightarrow 4_1^+$	338	340^{+420}_{-140}	315	295
8_1^+	1096.7	<5	$8_1^+ \rightarrow 6_1^+$	430	>206	349	308

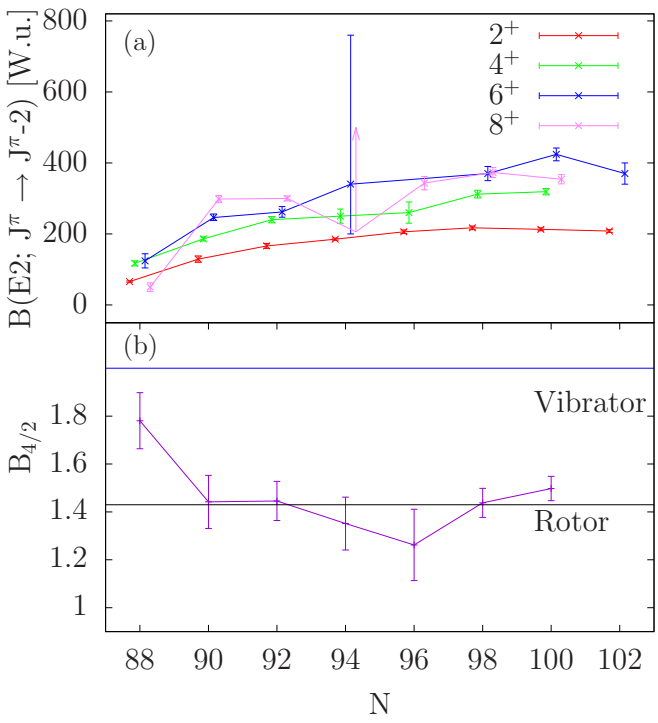

FIG. 8. Systematic plot of (a) $B(E2;J \rightarrow J-2)$ transition probabilities for the $^{156-170}$Er isotopes and (b) $B_{4/2} = B(E2;4_1^+ \rightarrow 2_1^+)/B(E2;2_1^+ \rightarrow 0_1^+)$ ratio. Results for $N = 94$ are obtained from this work and other data points are taken from Refs. [38–43]. Only a lower limit for the $B(E2;8_1^+ \rightarrow 6_1^+)$ value in ^{162}Er is given. Data points for $N = 94$ are slightly moved horizontally to improve readability.

where $\langle IK20|(I-2)K\rangle$ is the Clebsch-Gordan coefficient for an initial spin I, a projection of intrinsic angular momentum on the symmetry axis K coupled to a nuclear spin of $I-2$. Equation (6) is suited for transitions within a rotational band with Q_t in units of eb. For the yrast band of an even-even nucleus $K = 0$ can be assumed [48]. The intrinsic quadrupole moment is further connected to the quadrupole deformation parameter β_2 according to [21]

$$Q_t = \sqrt{\frac{16\pi}{5}}\frac{3}{4\pi}ZeR_0^2\beta_2. \tag{7}$$

In Eq. (7), Ze is the nuclear charge and R_0 the nuclear radius calculated via $R_0 = 1.2A^{1/3}$ fm. The uncertainties of Q_t and β_2 are calculated by error propagation through the uncertainties on the $B(E2)$ strengths given in Table I. The results of the calculation for $^{158-170}$Er are shown in Table II. A quadrupole moment of $Q_t = 6.98(6)\,e$b for ^{162}Er was calculated from the $B(E2;2_1^+ \rightarrow 0_1^+)$ value determined in the present work that corresponds to a deformation of $\beta_2 = 0.327(3)$. Following the same trend as the $B(E2;2_1^+ \rightarrow 0_1^+)$ the β_2 deformation reaches its maximum deformation at $N = 98$ and saturates, within uncertainty, around $N = 100$. Relativistic mean-field (RMF) calculations performed by Lalazissis *et al.* [49] show a similar evolution of β_2 in the chain of erbium isotopes, although slightly underestimating the magnitude of the deformation parameter. More recent calculations by Bonatsos *et al.* [50] in the proxy-SU(3) model also predict a smooth development of collectivity and a maximum of β deformation around neutron number 100, 102 with $\beta_2 \approx 0.32$.

Figure 8(b) shows the $B_{4/2} = B(E2;4_1^+ \rightarrow 2_1^+)/B(E2;2_1^+ \rightarrow 0_1^+)$ ratios as a function of neutron number for the Er isotopic chain. With $R_{4/2} = E(4_1^+)/E(2_1^+) = 3.23$, ^{162}Er is considered a statically deformed nucleus close the rigid rotor limit. The value for the lifetime of the 4_1^+ state allows to obtain the $B_{4/2}$ which is about 1.35 and fits well into systematic trend. A smooth trend with values around the rigid rotor limit ($B_{4/2} = 1.43$) for $90 \leqslant N \leqslant 100$ is observed with a small deviation for ^{164}Er as can also be seen in the dip of the $B(E2;4_1^+ \rightarrow 2_1^+)$ value in Fig. 8(a). Extending this information towards the midshell nucleus ^{172}Er is of high interest to gain a complete picture on the evolution of deformation of the Er isotopic chain.

TABLE II. Summary of $B(E2;2_1^+ \rightarrow 0_1^+)$ values in the Er isotopes with $90 \leqslant N \leqslant 102$, deduced quadrupole moments Q_t and deformation parameters β_2. Nuclear data for $^{158,160,164-170}$Er are taken from Refs. [39–43,51]. Theoretical calculations based on a relativistic mean-field (RMF) are taken from Ref. [49].

		$E_x(2_1^+)$	$B(E2)\downarrow$	Q_t	β_2	
N	Nucleus	[keV]	[W.u.]	[eb]	exp	RMF
90	^{158}Er	192.2	129(9))	5.7(2)	0.27(1)	0.229
92	^{160}Er	125.8	166(7)	6.6(1)	0.311(5)	0.266
94	^{162}Er	102.0	185(3)	6.98(6)	0.327(3)	0.289
96	^{164}Er	91.4	206(5)	7.43(8)	0.345(4)	0.305
98	^{166}Er	80.6	217(5)	7.70(5)	0.354(2)	0.319
100	^{168}Er	78.8	213(4)	7.68(5)	0.351(2)	0.333
102	^{170}Er	78.6	208(4)	7.68(5)	0.348(2)	0.339

B. CBS calculations

A suited description of the quadrupole collectivity of even-even nuclei in the rare-earth region can be reached using the Bohr Hamiltonian [21]:

$$H_B = T_{\rm vib} + T_{\rm rot} + V(\beta,\gamma). \tag{8}$$

Here, the kinetic energy term T is separated into vibrational and rotational part and β and γ are the quadrupole deformation parameters. By choosing a separable potential V such that $V(\beta,\gamma) = v(\beta) + u(\gamma)$, spherically and statically deformed nuclei can be described as analytic solutions of Eq. (8). The potential depending on the β degree of freedom can be described as an infinite square well with moving boundaries $0 \leqslant \beta_m < \beta_M$ [11]. Due to the properties of the potential, the wave function separates into $\Psi(\beta,\gamma,\theta_i) = \xi_L(\beta)\eta_K(\gamma)\mathcal{D}^L_{M,K}(\theta_i)$, where $\mathcal{D}$ represents the Wigner functions and θ_i being the Euler angles. η_K is defined in Ref. [4] and ξ_L is obtained by applying Eq. (8) and governed by the following differential equation:

$$-\frac{\hbar}{2B}\left[\frac{1}{\beta^4}\frac{\partial}{\partial\beta}\beta^4\frac{\partial}{\partial\beta} - \frac{1}{3\beta^2}L(L+1) + v(\beta)\right]\xi_L(\beta) = E\xi_L(\beta). \tag{9}$$

TABLE III. Summary of the model parameters of the CBS calculation (top) and IBM calculation (bottom) for ^{162}Er. Details see text.

CBS	r_β	$B\beta_M^2$	β_M	
	0.323	0.024	6.054	
IBM	ζ	χ	c	e_B [e^2b^2]
	0.73	−0.55	1.55	0.18

In Eq. (8), B describes the moment of inertia, L the orbital angular momentum, and E the eigenvalues of the eigenfunctions ξ_L. Introducing a new variable $z = \sqrt{E/(\hbar^2/2B)}/\beta$, the eigenvalues of Eq. (9) can be written as

$$E_{L,s} = \frac{\hbar^2}{2B\beta_M^2}\left(z_{L,s}^{r_\beta}\right)^2. \tag{10}$$

The energy scale is defined by the parameter $B\beta_M^2$. A phenomenon known as the centrifugal stretching results from the properties of the wave functions $\xi_{L,s}(\beta)$. With increasing orbital angular momentum L, the density of the wave function is pushed to higher quadrupole deformation β. Despite the fact that ^{162}Er has $R_{4/2} = 3.23$ which is very close to the rotational limit of 3.33, a significant centrifugal stretching in the order of 15% is observed for the $L = 10$ wave function.

For ^{162}Er, $r_\beta = 0.323$ is obtained in order to reproduce the excitation energies. A summary of the different model parameters is shown in the first part of Table III. The value for r_β is significantly larger than the one obtained for ^{160}Er ($r_\beta = 0.233$). This is in agreement with the assumption, that ^{162}Er is the first nucleus in the erbium chain of isotopes to show well-deformed rotational structure. Towards the midshell nucleus ^{172}Er the ratio increases to $r_\beta \approx 0.47$. A comparison between experimental and theoretical excitation energies in shown in Fig. 9 for Er isotopes with $92 \leqslant N \leqslant 104$. The deviations from the experimental values are below or around 1 keV for spins up to $J = 10$. Despite a slight deviation in the 12_1^+ states, the systematic evolution of excitation energies is very well reproduced by the CBS calculations. In Fig. 9(b), the excitation energies are plotted as a function of spin for ^{162}Er. The predictions by the SU(3) (rigid rotor) and X(5) solutions are also shown for comparison. From this plot it is evident that ^{162}Er can be seen as intermediate nucleus between X(5) and SU(3), thus, justifying the applicability of the CBS model. Furthermore, the effect of the centrifugal stretching is also visible from this trend. With increasing spin, the difference between the experimental energies and SU(3) limit become smaller compared to the X(5) limit.

Reduced transition probabilities in the framework of the CBS model can be calculated via [11]

$$\hat{T} = e_{\text{eff}}\hat{\beta}, \tag{11}$$

where e_{eff} represents the effective charge. The results are normalized to the $B(E2; 2_1^+ \rightarrow 0_1^+)$ value and are given in Table I. The transition rates for the higher-lying yrast states are well reproduced by the CBS calculations within uncertainties. The experimental $B(E2; 4_1^+ \rightarrow 2_1^+)$ value has a small uncertainty and the results of the CBS calculation is at the upper limits of the experimental value. For the $B(E2; 6_1^+ \rightarrow 4_1^+)$ strength, the experimental uncertainty is too high to draw any conclusions. This is due to the fact that the value is at the lower limit of the fast-timing technique and motivates further studies using different lifetime measurement techniques.

C. IBM calculations

The CBS calculations are limited to $\gamma = 0^\circ$ and the path between the X(5) and SU(3) points in the symmetry triangle. To gain a more complete picture, calculations are performed in the framework of the sd-IBM-1 [53], where no distinction between protons and neutrons is made. The following Hamiltonian is used:

$$H(\zeta, \chi) = c\left[(1-\zeta)\hat{n}_d - \frac{\zeta}{4N_B}\hat{Q}^\chi\hat{Q}^\chi\right], \tag{12}$$

known as the extended consistent Q formalism [54]. In Eq. (12), $\hat{n}_d = d^\dagger \cdot \tilde{d}$ is the d-boson number operator, $N_B = 13$ the boson number and $\hat{Q}^\chi$ the quadrupole operator defined as

$$\hat{Q}^\chi = (s^\dagger\tilde{d} + d^\dagger s) + \chi(d^\dagger\tilde{d})^{(2)}. \tag{13}$$

The quadrupole operator defined in Eq. (13) is related to the $E2$ transition probability $T(E2)$ via the effective boson charge

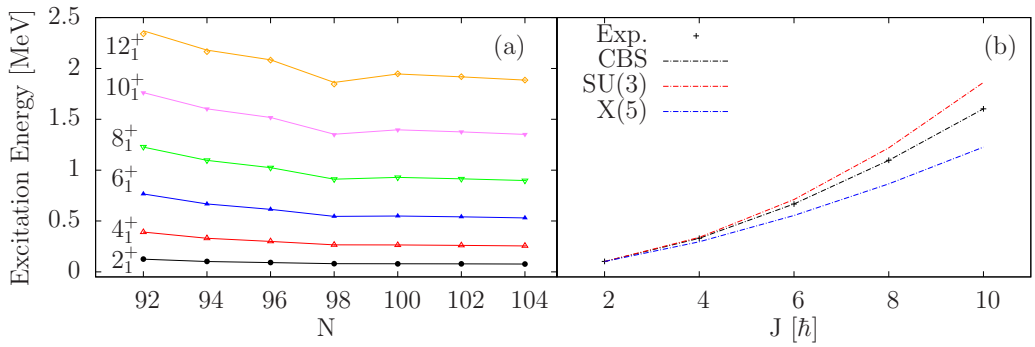

FIG. 9. (a) Excitation energies of yrast states up to $J^\pi = 12^+$ as a function of neutron number for Er isotopes. Data for $^{158,160,164-72}$Er are taken from Refs. [39–43,51,52]. The points represent experimental values and the data points connected by solid lines to guide the eye correspond to the results from the CBS calculation. (b) Excitation energy of yrast states as a function of spin J for ^{162}Er. The dashed lines represent theoretical calculations in the CBS model (black), SU(3) limit (red), and X(5) limit (blue).

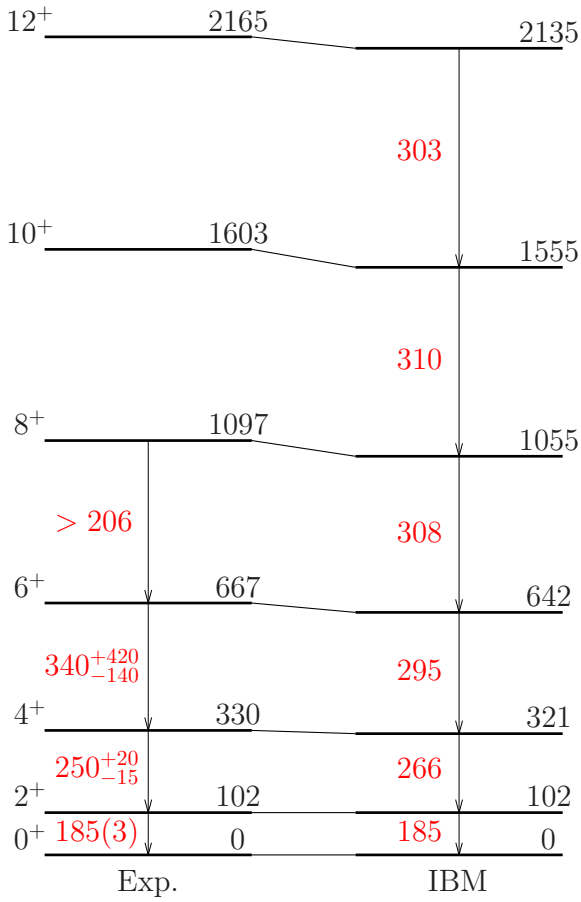

FIG. 10. Experimental (left) and theoretical (right) level scheme of yrast states in ^{162}Er up to $J = 12$. Energies are given in keV and $B(E2)$ values in W.u. are labeled in red. Theoretical energies and $B(E2)$ values are calculated in the framework of the sd-IBM-1, see text for details.

e_B according to

$$T(E2) = e_B Q. \tag{14}$$

The Hamiltonian in Eq. (12) involves two parameters ζ and χ plus a scaling factor. The SU(3) limit is given by $\zeta = 1$ and $\chi = -\sqrt{7}/2$. The calculations were performed using the computer code ARBMODEL [55]. The $R_{4/2}$ value close to the SU(3) limit suggests a ζ value close to one. A full parameter scan to reproduce excited states and transition probabilities in ^{162}Er showed that the parameters $\zeta = 0.73$ and $\chi = -0.55$ yield a good agreement with the experimental excitation energies. The scaling parameter was adjusted to reproduce $E_x(2_1^+) = 102$ keV. A summary of the IBM-1 parameters are given in the second part of Table III. The obtained parameters are consistent with the overall systematic of ζ and χ in this region [56]. The $\zeta = 0.73$ is consistent with the r_β value obtained in the CBS calculation but $\chi > -\sqrt{7}/2$ shows a small degree of γ softness that cannot be accounted for in the CBS model.

The results are shown in Fig. 10 together with the experimental values. The values show an overall consistency with the measured energies. A deviation below or around 50 keV is achieved for all the states with a maximum deviation of about 50 keV for the 10_1^+ state. The effective boson charge in units of e^2b^2 was chosen to be $e_B = 0.18\, e^2b^2$ in order to match the experimental $B(E2; 2_1^+ \rightarrow 0_1^+)$ value. The calculated transition probabilities are given in Table I. The resulting $B(E2)$ values match the experimental ones within uncertainties.

VI. SUMMARY

Lifetimes of low-lying excited states in ^{162}Er were measured using the γ-γ fast-timing technique. The half-life of the 2_1^+ state was remeasured and is consistent with previous measurements while improving its uncertainty. The lifetimes of the 4_1^+ and 6_1^+ state were measured for the first time and fit well into the systematic trend of the isotopic chain. Experimental results are well described using the CBS and the IBM. CBS calculations account for the varying degree of centrifugal stretching along the Er isotopic chain. sd-IBM-1 calculations support the description of ^{162}Er as a deformed rotor with a small degree of γ softness. Furthermore, the half-life of the $K^\pi = (7^-)$ isomer is remeasured with higher precision.

ACKNOWLEDGMENTS

The authors would like to thank the operator staff of the FN Tandem accelerator. This work was supported by the Deutsche Forschungsgemeinschaft (DFG) under Grant No. JO 391/16-2.

[1] R. F. Casten, Nucl. Phys. A **443**, 1 (1985).
[2] R. F. Casten and N. Zamfir, J. Phys. G **22**, 1521 (1999).
[3] F. Iachello, Phys. Rev. Lett. **85**, 3580 (2000).
[4] F. Iachello, Phys. Rev. Lett. **87**, 052502 (2001).
[5] M. A. Caprio, Phys. Rev. C **65**, 031304(R) (2002).
[6] F. Iachello, Phys. Rev. Lett. **91**, 132502 (2003).
[7] D. Bonatsos, D. Lenis, D. Petrellis, and P. A. Terziev, Phys. Lett. B **588**, 172 (2004).
[8] M. A. Caprio, Phys. Rev. C **69**, 044307 (2004).
[9] D. Bonatsos, D. Lenis, N. Minkov, D. Petrellis, P. P. Raychev, and P. A. Terziev, Phys. Rev. C **70**, 024305 (2004).
[10] L. Fortunato, Phys. Rev. C **70**, 011302(R) (2004).
[11] N. Pietralla and O. M. Gorbachenko, Phys. Rev. C **70**, 011304(R) (2004).
[12] D. Bonatsos, D. Lenis, D. Petrellis, P. A. Terziev, and I. Yigitoglu, Phys. Lett. B **621**, 102 (2005).
[13] D. Bonatsos, D. Lenis, D. Petrellis, P. A. Terziev, and I. Yigitoglu, Phys. Lett. B **632**, 238 (2006).
[14] E. A. McCutchan, D. Bonatsos, and N. V. Zamfir, Phys. Rev. C **74**, 034306 (2006).
[15] R. F. Casten and E. A. McCutchan, J. Phys. G **34**, R285 (2007).
[16] P. Cejnar, J. Jolie, and R. F. Casten, Rev. Mod. Phys. **82**, 2155 (2010).

[17] Y. Zhang, F. Pan, Y. A. Luo, and J. P. Draayer, Phys. Lett. B **751**, 423 (2015).
[18] R. Budaca and A. I. Budaca, Phys. Lett. B **759**, 349 (2016).
[19] Y. Zhang, F. Pan, Y.-X. Liu, Y. A. Luo, and J. P. Draayer, Phys. Rev. C **96**, 034323 (2017).
[20] V. Karayonchev, J.-M. Régis, J. Jolie, A. Blazhev, R. Altenkirch, S. Ansari, M. Dannhoff, F. Diel, A. Esmaylzadeh, C. Fransen, R.-B. Gerst, K. Moschner, C. Müller-Gatermann, N. Saed-Samii, S. Stegemann, N. Warr, and K. O. Zell, Phys. Rev. C **95**, 034316 (2017).
[21] A. Bohr and B. R. Mottelson, *Nuclear Structure, Vol. 1* (World Scientific, Singapore, 1969).
[22] M. A. Caprio, R. F. Casten, N. V. Zamfir, G. C. Ball, K. P. Jackson, P.-A. Amaudruz, and J.-C. Thomas, Phys. Rev. C **66**, 014307 (2002).
[23] V. A. Morozov, T. M. Muminov, and A. B. Khalikulov, Technical Report No. JINR P6-5201 (Joint Institute for Nuclear Research, Dubna, 1970).
[24] M. A. Caprio, N. V. Zamfir, E. A. McCutchan, R. F. Casten, Z. Berant, H. Amro, C. J. Barton, C. W. Beausang, D. S. Brenner, J. R. Cooper, R. L. Gill, G. Gürdal, A. A. Hecht, C. Hutter, R. Krücken, D. A. Meyer, J. R. Novak, N. Pietralla, P. H. Regan, and J. J. Ressler, Eur. Phys. J. A **16**, 177 (2003).
[25] R. M. Ronningen, R. B. Piercey, J. H. Hamilton, C. F. Maguire, A. V. Ramayya, H. Kawakami, B. van Nooijen, R. S. Grantham, W. K. Dagenhart, and L. L. Riedinger, Phys. Rev. C **16**, 2218 (1977).
[26] P. M. Walker and G. Dracoulis, Nature (London) **399**, 35 (1999).
[27] P. M. Walker and G. Dracoulis, Hyperfine Interact. **135**, 83 (2001).
[28] T. P. D. Swan, P. M. Walker, Zs. Podolyák, M. W. Reed, G. D. Dracoulis, G. J. Lane, T. Kibédi, and M. L. Smith, Phys. Rev. C **85**, 024313 (2012).
[29] A. Linnemann, Ph.D. thesis, University of Cologne, 2005.
[30] J.-M. Régis, N. Saed-Samii, M. Rudigier, S. Ansari, M. Dannhoff, A. Esmaylzadeh, C. Fransen, R.-B. Gerst, J. Jolie, V. Karayonchev, C. Müller-Gatermann, and S. Stegemann, Nucl. Instrum. Methods Phys. Res. A **823**, 72 (2016).
[31] J.-M. Régis, H. Mach, G. S. Simpson, J. Jolie, G. Pascovici, N. Saed-Samii, N. Warr, A. Bruce, J. Degenkolb, L. M. Fraile, C. Fransen, D. G. Ghita, S. Kisyov, U. Koester, A. Korgul, S. Lalkovski, N. Marginean, P. Mutti, B. Olaizola, Z. Podolyak, P. H. Regan, O. J. Roberts, M. Rudigier, L. Stroe, W. Urban, and D. Wilmsen, Nucl. Instrum. Methods Phys. Res. A **726**, 191 (2013).
[32] Z. Bay, Phys. Rev. **77**, 419 (1950).
[33] J.-M. Régis, G. Pascovici, J. Jolie, and M. Rudigier, Nucl. Instrum. Methods Phys. Res. A **622**, 83 (2010).
[34] J.-M. Régis, A. Esmaylzadeh, J. Jolie, V. Karayonchev, L. Knafla, U. Köster, Y. H. Kim, and E. Strub, Nucl. Instrum. Methods Phys. Res. A **955**, 163258 (2020).
[35] J. Bjerregård, B. Elbek, O. Hansen, and P. Salling, Nucl. Phys **44**, 280 (1963).
[36] G. Häfner, K. Moschner, A. Blazhev, P. Boutachkov, P. J. Davies, R. Wadsworth, F. Ameil, H. Baba, T. Bäck, M. Dewald, P. Doornenbal, T. Faestermann, A. Gengelbach, J. Gerl, R. Gernhäuser, S. Go, M. Górska, H. Grawe, E. Gregor, H. Hotaka, T. Isobe, D. G. Jenkins, J. Jolie, H. S. Jung, I. Kojouharov, N. Kurz, M. Lewitowicz, G. Lorusso, R. Lozeva, E. Merchan, F. Naqvi, H. Nishibata, D. Nishimura, S. Nishimura, N. Pietralla, H. Schaffner, P.-A. Söderström, K. Steiger, T. Sumikama, J. Taprogge, P. Thöle, H. Watanbe, N. Warr, V. Werner, Z. Y. Xu, A. Yagi, K. Yoshinaga, and Y. Zhu, Phys. Rev. C **100**, 024302 (2019).
[37] F. S. Stephens, Rev. Mod. Phys. **47**, 43 (1975).
[38] C. W. Reich, Nucl. Data Sheets **113**, 2537 (2012).
[39] N. Nica, Nucl. Data Sheets **141**, 1 (2017).
[40] N. Nica, Nucl. Data Sheets **105**, 557 (2005).
[41] B. Singh and J. Chen, Nucl. Data Sheets **147**, 1 (2018).
[42] C. M. Baglin, Nucl. Data Sheets **109**, 1103 (2008).
[43] C. M. Baglin, Nucl. Data Sheets **111**, 1807 (2010).
[44] R. L. Canavan, M. Rudigier, P. H. Regan, M. Lebois, J. N. Wilson, N. Jovancevic, P.-A. Söderström, S. M. Collins, D. Thisse, J. Benito, S. Bottoni, M. Brunet, N. Cieplicka-Oryńczak, S. Courtin, D. T. Doherty, L. M. Fraile, K. Hadyńska-Klęk, G. Häfner, M. Heine, Ł. W. Iskra, V. Karayonchev, A. Kennington, P. Koseoglou, G. Lotay, G. Lorusso, M. Nakhostin, C. R. Niţă, S. Oberstedt, Zs. Podolyák, L. Qi, J.-M. Régis, V. Sánchez-Tembleque, R. Shearman, V. Vedia, and W. Witt, Phys. Rev. C **101**, 024313 (2020).
[45] P.-A. Söderström, J. Nyberg, P. H. Regan, A. Algora, G. de Angelis, S. F. Ashley, S. Aydin, D. Bazzacco, R. J. Casperson, W. N. Catford, J. Cederkäll, R. Chapman, L. Corradi, C. Fahlander, E. Farnea, E. Fioretto, S. J. Freeman, A. Gadea, W. Gelletly, A. Gottardo, E. Grodner, C. Y. He, G. A. Jones, K. Keyes, M. Labiche, X. Liang, Z. Liu, S. Lunardi, N. Mărginean, P. Mason, R. Menegazzo, D. Mengoni, G. Montagnoli, D. Napoli, J. Ollier, S. Pietri, Zs. Podolyák, G. Pollarolo, F. Recchia, E. Şahin, F. Scarlassara, R. Silvestri, J. F. Smith, K.-M. Spohr, S. J. Steer, A. M. Stefanini, S. Szilner, N. J. Thompson, G. M. Tveten, C. A. Ur, J. J. Valiente-Dobón, V. Werner, S. J. Williams, F. R. Xu, and J. Y. Zhu, Phys. Rev. C **81**, 034310 (2010).
[46] R. F. Casten, K. Heyde, and B. Wolf, Phys. Lett. B **208**, 33 (1988).
[47] A. G. Smith, J. L. Durell, W. R. Phillips, W. Urban, P. Sarriguren, and I. Ahmad, Phys. Rev. C **86**, 014321 (2012).
[48] A. Bohr and B. R. Mottelson, *Nuclear Structure, Vol. 2* (World Scientific, Singapore, 1975).
[49] G. A. Lalazissis, M. M. Sharma, and P. Ring, Nucl. Phys. A **597**, 35 (1996).
[50] D. Bonatsos, I. E. Assimakis, N. Minkov, A. Martinou, S. Sarantopoulou, R. B. Cakirli, R. F. Casten, and K. Blaum, Phys. Rev. C **95**, 064326 (2017).
[51] C. M. Baglin, E. A. McCutchan, S. Basunia, and E. Browne, Nucl. Data Sheets **153**, 1 (2018).
[52] B. Singh, Nucl. Data Sheets **75**, 199 (1995).
[53] A. Arima and F. Iachello, Phys. Rev. Lett. **35**, 1069 (1975).
[54] D. D. Warner and R. F. Casten, Phys. Rev. Lett. **48**, 1385 (1982).
[55] S. Heinze, Ph.D. thesis, University of Cologne, 2008.
[56] E. A. McCutchan, N. V. Zamfir, and R. F. Casten, Phys. Rev. C **69**, 064306 (2004).